Proceedings of HT2008
ASME Summer Heat Transfer Conference
August 10-14, 2008, Jacksonville, Fl, USA

HT2008-56280

Validation of Mist/Steam Cooling CFD model in a Horizontal Tube

T. S. Dhanasekaran and Ting Wang
Energy Conversion and Conservation Center
University of New Orleans
New Orleans, Louisiana, USA

ABSTRACT

Mist cooling concept has been considered for cooling turbine airfoils for many years. This concept has been proven experimentally as an effective method to significantly enhance the cooling effectiveness with several fundamental studies in the laboratory under low pressure and temperature conditions. However, it is not certain the same performance can be harnessed in the real gas turbine environment under the condition of elevated temperature, pressure, heat flux, and Reynolds number. This paper aims at validating a CFD model against experimental results in a circular tube and then applies the validated CFD model to simulate mist/steam cooling performance at elevated gas turbine working conditions. The results show that the standard k-ε and a RSM turbulence models are the best-suited model for this application. The mist with smaller droplet diameter is found achieving higher cooling enhancement than the flows with bigger droplets, while mist with a distributed droplet size matches the data slightest better than with uniform droplets. Both the wall-film and the reflect droplet boundary conditions are employed and their effects on the cooling result is not significant at the studied cases. The validated CFD model can predict the wall temperature within 2% in steam-only flow and 5% in the mist/steam flow. Applying the calibrated CFD model to the actual gas turbine working environment shows that the mist/steam cooling technique could harness an average 50-100% cooling enhancement.

Keywords: Mist cooling, heat transfer enhancement, two-phase flow, gas turbine blade cooling

INTRODUCTION

Closed-loop steam cooling has been adopted by two major gas turbine manufacturers for their heavy-frame advanced turbine systems (ATS) engines ([1-3]). The major advantage of the closed-loop steam cooling is that it can eliminate the need for film cooling. According to Bannister [4], as the turbine inlet temperature is raised to 1400^0C, excessive film cooling is the major obstacle to a further increase in gas turbine thermal efficiency. This is because as the cooling air is injected from the airfoil into the main hot gas flow, it interferes with the main flow field and subsequently causes aerodynamic and thermal losses. In the meantime, less air is available for combustion and therefore the work output will be reduced. Furthermore, excessive film cooling will force the combustion temperature to be raised in order to achieve higher turbine inlet temperature and further compound the issue of reducing NOx and controlling emissions.

As a result, for the heavy frame ATS, using the closed-loop steam cooling scheme allows achievement of a higher thermal efficiency than those using air film cooling [5]. One of the most challenging problems of closed-loop steam cooling is that a very large amount of steam will be needed [3,6]. The reason is that in order to eliminate film cooling, the coolant side heat transfer coefficient must be greatly increased (to about 8,000 – 10,000 W/m^2K). To reach such high heat transfer coefficients, a very high steam Reynolds number (thus a very high steam flow rate) must be maintained. Drawing this large amount of steam out from the bottom steam cycle would decrease the thermal efficiency of the bottom steam turbines since the normal steam expansion process would be interrupted [7]. Furthermore, high steam rate will significantly increase the pressure losses.

In order to address the above issues, the concept of controlled closed-loop mist/steam cooling was introduced and verified with extensive basic experiments on a horizontal tube [8,9], a 180-degree curved tube [10], impingement jets on a flat surface [11], and impingement jets on a curved surface [12]. Typically, an average cooling enhancement of 50 - 100% was achieved by injecting 1-3% (wt.) mist into the steam flow. Very high local cooling enhancement of 200 - 300% was observed in the tube and on a flat surface, and cooling enhancement above 500% was observed when steam flow passed the 90-degree bend.

The experimental and numerical heat transfer results of air-mist dispersed flows around cylinders [13-14], wedge-shaped bodies [15] and plates [16-17] have also shown the predominant effect of mist in the cooling enhancement. Similar effects have been observed in the vapour-droplet

flow in the duct [18-19]. The concept of using small water droplets (mist) to enhance cooling in gas turbine hot components is not new. More detailed literature reviews can be found in Guo et al.[8] and Li et al. [11].

The present investigation focuses on validating the CFD model with the experimental data taken in the laboratory in a horizontal tube by Guo et al. [8,9] under low temperature and pressure conditions. Their results showed that the mist cooling enhancement reached an average 200-300% under lower heat flux conditions, but it deteriorated to about 50 % under higher heat flux conditions. It was concerned then that the mist cooling might not be beneficial under the elevated wall heat flux condition in the real gas turbine operating environment. However, they further increased the Reynolds number and observed the cooling enhancement returned back to above 100%. Based on this finding, Guo et al. [9] hypothesized that the mist cooling could be still attractive under elevated gas turbine operating condition because the Reynolds number is high and the steam properties will change in favor of mist cooling in the actual gas turbine environment. The objective of this paper is to investigate whether their hypothesis is correct by validating a CFD model with their experimental results and then apply the validated CFD model to predict the potential mist/steam cooling under actual gas turbine operating conditions.

NUMERICAL MODEL

Test Section

The test section schematic diagram of the horizontal tube used by Guo et al. [8] is shown in Fig. 1. The locations of the thermocouples and heated portion of the tube can be seen from the figure. The temperature measurements were taken at 7 locations along the heated pipe (Fig. 1). The steam was blended in a mixing chamber with fine water droplets generated by an atomizing system before entering into the test section. The mixing chamber was designed to allow larger droplets to deposit in the chamber and only a well-mixed mist/steam flow emerged from the chamber with the water droplets suspending in the steam flow. The steam at saturation pressure of 1.5-1.6 bar was maintained at the inlet to the test section. Additional details on the experimental test set-up can be obtained from reference [8].

The geometry details of the computational domain are shown in Fig. 2. The horizontal tube inner diameter is 22.2mm. Instead of only simulating the heated test section, similar to the experimental set up, the computational domain includes a 60 mm unheated section leading to the heated section and following by a 10 mm unheated section. This will allow the velocity profile at the inlet of the heated section very close to the actual velocity profile in the experiment. The test section was heated by a high-current DC power supply system. It should be noted again that the mist was not generated by an atomizer at the inlet to the heated test section; rather, the mist was generated and mixed with saturated steam in a mixer approximate 3 feet away from the test section and was then transported to the settling chamber. This process provides a true mist flow with liquid droplets suspending in the main flow.

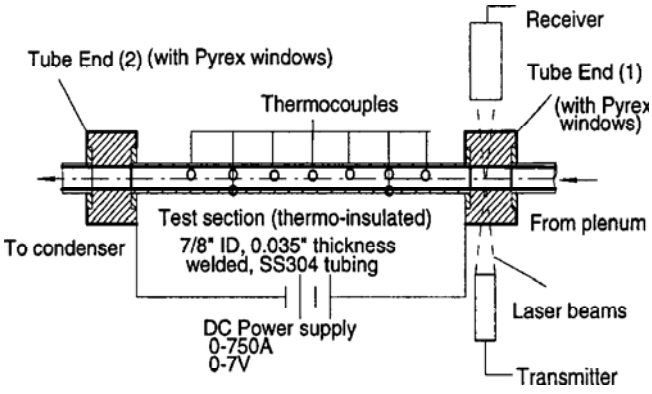

Figure 1 Experimental set-up (Guo et al. [8])

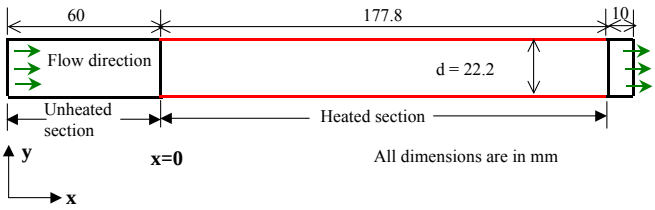

Figure 2 Geometry details of the computational domain (no to scale). X=0 is set at the starting point of heated section.

Numerical Method

A feasible method to simulate the steam flow with mist injection is to consider the droplets as a discrete phase since the volume fraction of the liquid is usually small (e.g. 5% mist by weight gives approximately 0.08% in volume.) The trajectories of the discret phase (droplets) are calculated by the Lagrangian method by tracking each droplet from its origin. The impact of the droplets on the continuous phase is considered as source terms to the governing equations of mass, momentum and energy. Two components (water and water vapor) are simulated in the simulation. Various turbulence models are used with enhanced near-wall treatment to the continuous phase (stream).

Governing Equations

The 3-D time-averaged steady-state Navier-Stokes equations as well as equations for mass and energy are solved. The governing equations for conservation of mass, momentum, and energy are given as:

$$\frac{\partial}{\partial x_i}\left(\rho u_i\right) = S_m \tag{1}$$

$$\frac{\partial}{\partial x_i}\left(\rho u_i u_j\right) = \rho \vec{g}_j - \frac{\partial P}{\partial x_j} + \frac{\partial}{\partial x_i}\left(\tau_{ij} - \rho\overline{u'_i u'_j}\right) + F_j \tag{2}$$

$$\frac{\partial}{\partial x_i}\left(\rho c_p u_i T\right)=\frac{\partial}{\partial x_i}\left(\lambda\frac{\partial T}{\partial x_i}-\rho c_p\overline{u'_i\,T'}\right)+\mu\Phi+S_h \tag{3}$$

where τ_{ij} is the symmetric stress tensor defined as

$$\tau_{ij}=\mu\left(\frac{\partial u_j}{\partial x_i}+\frac{\partial u_i}{\partial x_j}-\frac{2}{3}\delta_{ij}\frac{\partial u_k}{\partial x_k}\right) \tag{4}$$

The source terms (S_m, F_j and S_h) are used to include the contribution from the dispersed phase. $\mu\Phi$ is the viscous dissipation.

In mist/air cooling, water droplets evaporate, and the vapor diffuses and is transported into its surrounding flow. Different from the mist/air flow, no species transport equation is used in the mist/steam flow since steam is the only main flow medium.

The terms of $\rho\overline{u'_i u'_j}$ and $\rho c_p\overline{u'_i T'}$, represent the Reynolds stresses and turbulent heat fluxes. The Reynolds number of the main flow (based on the tube diameter and the inlet condition) is about 20,000 in this study.

Turbulence Models

Standard k-ε Model – The standard k-ε model, which, based on the Boussinesq hypothesis, relates the Reynolds stresses to the mean velocity as

$$-\rho\overline{u'_i u'_j}=\mu_t\left(\frac{\partial u_i}{\partial x_j}+\frac{\partial u_j}{\partial x_i}\right)-\frac{2}{3}\rho k\delta_{ij} \tag{5}$$

The turbulent viscosity, μ_t is given by

$$\mu_t=\rho C_\mu k^2/\varepsilon \tag{6}$$

where C_μ is a constant. The equations for the turbulent kinetic energy (k) and the dissipation rate (ε) are:

$$\frac{\partial}{\partial x_i}\left(\rho u_i k\right)=\frac{\partial}{\partial x_i}\left[\left(\mu+\frac{\mu_t}{\sigma_k}\right)\frac{\partial k}{\partial x_i}\right]+G_k-\rho\varepsilon\,. \tag{7}$$

$$\frac{\partial}{\partial x_i}\left(\rho u_i \varepsilon\right)=\frac{\partial}{\partial x_i}\left[\left(\mu+\frac{\mu_t}{\sigma_\varepsilon}\right)\frac{\partial \varepsilon}{\partial x_i}\right]+C_{1\varepsilon}G_k\frac{\varepsilon}{k}-C_{2\varepsilon}\rho\frac{\varepsilon^2}{k}\,. \tag{8}$$

The term G_k is the generation of turbulent kinetic energy due to the mean velocity gradients.

The turbulent heat flux can be modeled with the turbulent heat conductivity (λ_t).

$$\rho c_p\overline{u'_i T'}=-\lambda_t\frac{\partial T}{\partial x_i}=-c_p\frac{\mu_t}{Pr_t}\frac{\partial T}{\partial x_i}\,, \tag{9}$$

The constants $C_{1\varepsilon}$, $C_{2\varepsilon}$, C_μ, σ_k, and σ_ε used are: $C_{1\varepsilon}$= 1.44, $C_{2\varepsilon}$ = 1.92, C_μ = 0.09, σ_k = 1.0, σ_ε =1.3 [20]. The turbulent Prandtl number, Pr_t, is set to 0.85,.

Enhanced Wall Function – The above k-ε model is mainly valid for a high Reynolds number fully turbulent flow. Special treatment is needed in the region close to the wall. The enhanced wall function is one of several methods that model the near-wall flow. In the enhanced wall treatment, a two-layer model is combined with the wall functions. The whole domain is separated into a viscosity-affected region and a fully turbulent region by defining a turbulent Reynolds number, Re_y,

$$Re_y=yk^{1/2}/\nu \tag{10}$$

where y is the distance from the wall. The standard k-ε model is used in the fully turbulent region where $Re_y > 200$, and the one-equation model of Wolfstein [21] is used in the viscosity-affected region with $Re_y < 200$. The turbulent viscosities calculated from these two regions are blended with a blending function (θ) to smoothen the transition.

$$\mu_{t,enhanced}=\theta\mu_t+(1-\theta)\mu_{t,l} \tag{11}$$

where μ_t is the viscosity from the k-ε model of high Reynolds number, and $\mu_{t,l}$ is the viscosity from the near-wall one-equation model. The blending function is equal to 0 at the wall and 1 in the fully turbulent region. The linear (laminar) and logarithmic (turbulent) laws of the wall are also blended to make the wall functions applicable throughout the entire near-wall region.

Reynolds Stress Model – In order to deal the flow with anisotropic and nonequilibrium with multiscaled integral and dissipation length scales, a Reynolds stress model (RSM); a second-moment closure, is considered in this study. The Reynolds stress transport equation is given as

$$\begin{aligned}\frac{\partial}{\partial x_k}\left(\rho u_k\overline{u'_i u'_j}\right)=&-\frac{\partial}{\partial x_k}\left[\rho u_k\overline{u'_i u'_j u'_k}+\overline{P(\delta_{kj}u'_i+\delta_{ik}u'_j)}+\mu\frac{\partial}{\partial x_k}\left(\overline{u'_i u'_j}\right)\right]\\&-\rho\left(\overline{u'_i u'_k}\frac{\partial u_j}{\partial x_k}+\overline{u'_j u'_k}\frac{\partial u_i}{\partial x_k}\right)+\overline{P\left(\frac{\partial u'_i}{\partial x_j}+\frac{\partial u'_j}{\partial x_i}\right)}-2\mu\overline{\frac{\partial u'_i}{\partial x_k}\frac{\partial u'_j}{\partial x_k}}\end{aligned} \tag{12}$$

The diffusive term on the right-hand side can be modeled as

$$\begin{aligned}&-\frac{\partial}{\partial x_k}\left[\rho u_k\overline{u'_i u'_j u'_k}+\overline{P(\delta_{kj}u'_i+\delta_{ik}u'_j)}+\mu\frac{\partial}{\partial x_k}\left(\overline{u'_i u'_j}\right)\right]\\&\quad=\frac{\partial}{\partial x_k}\left(\frac{\mu_t}{\sigma_k}\frac{\partial}{\partial x_k}\left(\overline{u'_i u'_j}\right)\right)\end{aligned} \tag{13}$$

The second term on the right-hand side of Eq. (12) is the production term, and it is notated as G_{ij}.

$$G_{ij}=-\rho\left(\overline{u'_i u'_k}\frac{\partial u_j}{\partial x_k}+\overline{u'_j u'_k}\frac{\partial u_i}{\partial x_k}\right) \tag{14}$$

The third term is the pressure-strain term, which can be modeled as:

$$\overline{P\left(\frac{\partial u'_i}{\partial x_j}+\frac{\partial u'_j}{\partial x_i}\right)}=C_1\rho\frac{\varepsilon}{k}\left(\overline{u'_i u'_j}-\frac{2}{3}\delta_{ij}k\right)-C_2\left[A_{ij}-\frac{1}{3}\delta_{ij}A_{kk}\right] \tag{15}$$

where $A_{ij}=G_{ij}-\frac{\partial}{\partial x_k}\left(\rho u_k\overline{u'_i u'_j}\right)$. The constants C_1 and C_2 are 1.8 and 0.6, respectively. By assuming the dissipation is isotropic, the last term in Eq. (12) can be approximated by:

$$2\mu\overline{\frac{\partial u_i'}{\partial x_k}\frac{\partial u_j'}{\partial x_k}} = \frac{2}{3}\delta_{ij}\rho\varepsilon \quad (16)$$

Modeling of the turbulent heat flux is similar as in the k-ε model. The turbulent kinetic energy and its dissipation rate can be calculated from the Reynolds stresses.

Other Models – Ignoring details here, the turbulence models adopted in this study also include RNG k-ε model, k-ω model, and the shear-stress transport (SST) k-ω model. The constants used in these models can be seen in reference [22]. The RNG k-ε model was derived using renormalization group theory [23]. It has an additional term in the ε-equation to improve the accuracy and hence suitable for wider class of flows including rapidly strained flows. The effective viscosity is used to account for low-Reynolds-number effect. Theoretically, this model is more accurate and reliable than the standard k-ε model. The standard k-ω model is an empirical model based on transport equations for the turbulent kinetic energy (k) and the specific dissipation rate (ω), which can also be considered as the ratio of ε to k [24]. The low-Reynolds-number effect is accounted for in the k-ω model. The SST model is a mixture of the k-ω model and the k-ε model: close to the wall it becomes the k-ω model while in the far field the k-ε model is applied [25].

Discrete -Phase Model (Water Droplets)

Droplet Flow and Heat Transfer – Based on Newton's 2nd Law, the droplet motion in airflow can be formulated by

$$m_p d\mathbf{v_p}/dt = \sum \mathbf{F} \quad (17)$$

where $\mathbf{v_p}$ is the droplet velocity (vector). The right-hand side is the combined force acting on the droplet, which normally includes the hydrodynamic drag, gravity, and other forces such as Saffman's lift force [26], thermophoretic force [27], and Brownian force [28], etc.

Without considering the radiation heat transfer, droplet's heat transfer depends on convection and evaporation as given in the following equation.

$$m_p c_p \frac{dT}{dt} = \pi d^2 h(T_\infty - T) + \frac{dm_p}{dt} h_{fg} \quad (18)$$

where h_{fg} is the latent heat. The convective heat transfer coefficient (h) can be obtained with an empirical correlation [29 and 30]:

$$Nu_d = \frac{hd}{\lambda} = 2.0 + 0.6\,Re_d^{0.5}\,Pr^{0.33} \quad (19)$$

where Nu_d is the Nusselt number, and Pr is the Prandtl number.

Theoretically, evaporation can occur at two stages: (a) when the temperature is higher than the saturation temperature (based on local water vapor concentration), water evaporates, and the evaporation is controlled by the water vapor partial pressure until 100% relative humidity is achieved; (b) when the boiling temperature (determined by the air-water mixture pressure) is reached, water continues to evaporate. In this study, the main flow medium is steam, so the evaporation of the water droplets is not controlled by the partial water vapor (as in the mist/air flow), rather it is controlled by the total pressure of the steam flow, i.e. by the boiling temperature as in [31]:

$$-\frac{dm_p}{dt} = \pi d^2 \left(\frac{\lambda}{d}\right)(2.0 + 0.46 Re_d^{0.5}) \ln\left(1 + c_p(T_\infty - T)/h_{fg}\right)/c_p \quad (20)$$

where c_p is the specific heat of the bulk flow.

Stochastic Particle Tracking – The turbulence models discussed above can only obtain time-averaged velocity. Using this velocity to trace the droplet will result in an averaged trajectory. In a real flow, the instantaneous velocity fluctuation would make the droplet move around this averaged track. However, the instantaneous velocity is not simulated in the current computation because the turbulence is modeled in time-averaged terms. One way to simulate the instantaneous turbulent effect on droplet dispersion is to "improvise" the random turbulent fluctuation by using the stochastic tracking scheme [22]. Basically, the droplet trajectories are calculated by imposing the instantaneous flow velocity ($\bar{u} + u'$) rather than the average velocity ($\bar{u}$). The velocity fluctuation is then given as:

$$u' = \zeta\left(\overline{u'^2}\right)^{0.5} = \zeta(2k/3)^{0.5} \quad (21)$$

where ζ is a normally distributed random number. This velocity will apply during the characteristic lifetime of the eddy (t_e), which is a time scale calculated from the turbulent kinetic energy and dissipation rate (t_e = 0.3 k/ε). The time scale varies from case to case and it is essential that an adequate time scale be provided in the calculation [22]. A typical value in this study calculated from empirical formula (0.3 k/ε) is about 0.05 seconds. After this time period, instantaneous velocity will be updated with a new ζ value until a full trajectory is obtained. Note, when the RSM model is used, the velocity fluctuation is independently decided in each direction. When the stochastic tracking is applied, the basic interaction between droplets and continuous phase stays the same, which is accounted by the source terms in the conservation equations. The source terms are not directly but rather indirectly affected by the stochastic method; so formulation of the source terms is not affected by implementing the stochastic tracking method. For example, the drag force between a water droplet and the steam flow depends on the slip velocity calculated by the averaged Navier-Stokes equations. When the stochastic tracking method is used, a random velocity fluctuation is imposed at an instant of time, and the drag force will be calculated based on this instantaneous slip velocity. The source term associated with this instantaneous drag force enters into the momentum equation without any additional formulation. For a steady-state calculation, the "instant of time" means "each iteration step."

Influence of Various Forces Acting on the Droplets – As explained previously, the prediction of trajectory of a discrete phase particle is achieved by integrating the force balance on the particle. The dominant main forces are drag and gravitational. In addition to the main forces, secondary forces like thermophoretic, Brownian and Saffman are included in the computation. Saffman force [26] concerns a sphere moving in a shear field. It is perpendicular to the direction of flow, originating from the inertia effects in the viscous flow around the particle. It can be given as:

$$F_{saff} = 1.615\rho\nu^{0.5}(u_g - u_p)(du/dn)^{0.5} \quad (22)$$

where du/dn is the gradient of the tangential velocity. It is valid only when $Re_p << 1$.

The thermophoretic force arises from asymmetrical interactions between a particle and the surrounding fluid molecules due to temperature gradient. This force tends to repel particles or droplets from a high temperature region to a low temperature region. The following equation can be used to model this force:

$$F_n = -K\frac{1}{m_p T}\frac{\partial T}{\partial n} \quad (23)$$

More details can be found in Talbot et al. [27]

Brownian force considers the random motion of a small particle suspended in a fluid, which results from the instantaneous impact of fluid molecules. It can be modeled as a Gaussian white noise process with spectral intensity given by [28]. Instead of investigating which forces are dominant and should be considered, all forces are included in this study.

Boundary Conditions

Continuous flow (Steam) – The steam is considered as a continuous flow and mist is considered as a discrete flow in the model. The mass flow rate (0.0033 kg/s) is assigned as the inlet condition which gives the inlet velocity of 12 m/sec and the Reynolds number of 20,000 based on tube diameter. The saturated temperature of steam at the inlet is 115^{o}C. At the heated tube section heat flux of 14,000 W/m^2 is applied. The non-slip boundary condition is assigned at all the walls and unheated tubes are assigned as adiabatic walls. The inlet turbulence intensity is specified as 3% as observed in the experiment. The flow exit of computational domain is assumed to be at a constant pressure of 1 atm.

Discrete flow (mist) – The fine water droplet with both the uniform and distributed droplet diameters are used to validate the CFD model. A total number of 2,000 injection locations with 20 injection streams at each injection location are deployed at the inlet. A mass concentration ratio (mist/steam) of 5.7% is assigned.

Discrete phase wall boundary condition – When the droplet reaches the wall the fact of the trajectory is determined from the discrete phase wall boundary condition. Each droplet when it approaches the wall can undergo any one of the facts [22] based on the condition of the wall: dry or flooded.

In case of dry wall, the droplets have three major regimes including reflect, break-up and trap. According to Watchers et al. [32], the regimes depend on the incoming Weber number of the droplet. Here, the Weber number is the ratio of kinetic energy of a droplet to the surface energy of a droplet ($We = \rho\, d_d\, v_d\, /\sigma$). It was shown from the experimental results that the droplet with incoming Weber number (We_{in}) less than 10 reflects elastically with nearly same outgoing Weber number (We_{out}). As the incoming We increased further to $We_{in} > 80$, the droplet falls into disintegration region which leads to breakup of the droplet to several small droplets. In the transition region of $30<We<80$, the droplet has the possibility of either reflecting or breaking-up. Apart from the above two facts, the droplets can be trapped by the superheated wall also. In this case the trajectory calculations are terminated and particles' entire mass instantaneously passes into the vapor phase and enters the cell adjacent to the boundary.

On the other hand, when the droplets impinge on the flooded wall, it has the chance for four different regimes including splashing, spread, rebound and sticking as shown in Fig. 3. Harlow and Shannon [33] applied the marker-and-cell (MAC) technique to obtain finite difference solutions to the Navier-stokes equations for a viscous, incompressible liquid droplet impinging on a flat surface with and without liquid films. Even though the technique captures much of physics of drop-film interactions, it requires higher computational effort. Bai and Gosman [34] developed a spray impingement model which was formulated on the basis of literature findings and mass, momentum and energy conservation constraints. In their study the secondary droplets resulting from splashing had the distribution of sizes and velocities by analyzing the relevant impingement regimes and the associated post-impingement characteristics. The rebound velocity was calculated from the following equations.

$$V'_{td} = (5/7)\, V_{td} \quad (24)$$

$$V'_{nd} = -e\, V_{nd} \quad (25)$$

where V_{td} is the initial tangential velocity, V_{nd} is the initial normal velocity, V'_{td} is the rebounding tangential velocity, V'_{nd} is the rebounding normal velocity and the expression e is the function of the impingement angle. For the spread regime, the arriving drops are assumed to coalesce to form a local film. Within the splashing regime, it is assumed that two droplets of equal mass are ejected from the liquid film at a randomly determined in-plane angle. The ratio of mass splashed to the incident drop mass is determined to vary between 0.2 to 1.1 according to the experimental work of Yarin and Weiss [35]. The total number of splashed droplets is determined from a curve-fit of Stow and Stainer's [36] data. Using mass conservation the droplet diameters are then determined.

The wall film model used in this study is based on the work of Stanton et al. [37] and O'Rourke et al. [38]. The

four regimes, stick, rebound, spread, and splash are based on the impact energy and wall temperature. Below the boiling temperature of the liquid, the impinging droplet can either stick, spread or splash, while above the boiling temperature, the particle can either rebound or splash. The impact energy is defined by

$$E^2 = (\rho V_r^2 d_d / \sigma) [1/(\min (h_0 / d_d, 1) + \delta_{bl} / d_d] \quad (26)$$

where V_r is the relative velocity of particle in the frame of the wall and δ_{bl} is the boundary layer thickness. The sticking regime is applied when the value of E becomes less than 16. Splashing occurs when the impingement energy is above a critical E value of E_{cr} = 57.7. The splashing algorithm was followed as described in Stanton et al. [37].

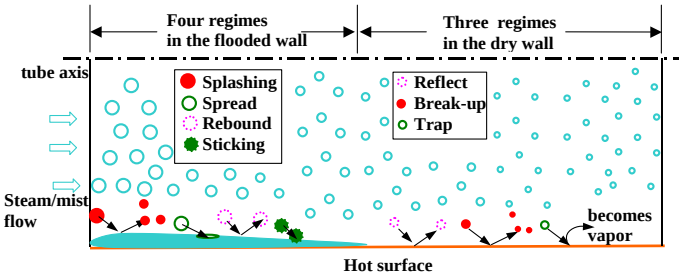

Figure 3 Droplet-wall interaction model

Computational Elements

The computational domain has been discretized to fine cells to conduct the simulation. Figure 4 shows the computational grid of the horizontal tube, which contains the total number of 0.5 million elements. The domain is completely constructed by hexahedral elements. To accurately predict possible recirculation, separation, and reattachment zones, the cells have been clustered towards the wall to obtain appropriate y+ value less than 1.

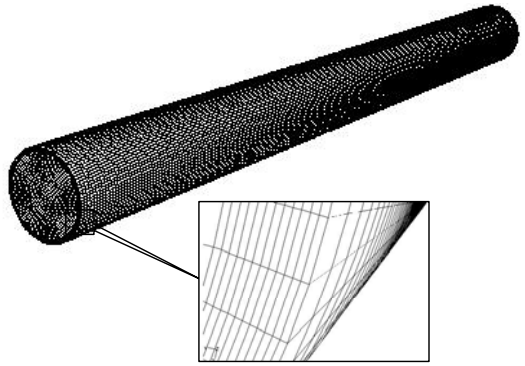

Figure 4 Computational domain and the grid. Near-wall mesh achieves $y^+ \approx 1$.

The computation has been carried out using the commercial CFD software FLUENT (Version 6.2.16) from Ansys, Inc. The simulation uses the segregated solver, which employs an implicit pressure-correction scheme and decouples the momentum and energy equations. The SIMPLE algorithm is used to couple the pressure and velocity. Second order upwind scheme is selected for spatial discretization of the convective terms. The second order accuracy is obtained by calculating quantities at cell faces using multidimensional linear reconstruction approach [22]. The computation is conducted for the steam field (continuous phase) first. After obtaining an approximate converged flow field of the steam, the dispersed phase of droplet trajectories are calculated. At the same time, drag, heat and mass transfer between the droplets and the steam flow are calculated. Variable property values are calculated using polynomial equations for steam and piecewise approximation for water droplets. It was discovered that the property database for water vapor and steam in Fluent is not sufficient and gives unreasonable results such as predicting temperature lower than Wet Bulb temperature after water droplet evaporation. A more detailed database has been incorporated through Function statement.

Iterations proceed alternatively between the continuous and discrete phases. Ten iterations in the continuous phase are conducted between two iterations of the discrete phase. Converged results are obtained after the residuals satisfy mass residual of 10^{-4}, energy residual of 10^{-6}, and momentum and turbulence kinetic energy residuals of 10^{-5}. These residuals are the summation of the imbalance in each cell, scaled by a representative for the flow rate. The computation was carried out in parallel processing on two dual-core Pentium clusters with 10 nodes and 6 nodes, respectively.

Grid Sensitivity Study

A grid sensitivity test has been carried out with 0.1, 0.3 and 0.5 million cells as shown in Fig. 5. The test verified that the wall temperature distribution negligibly affected by number of cells beyond 0.3 million cells. Hence, the computational domain with 0.5 million cells have been chosen to carry out further investigations.

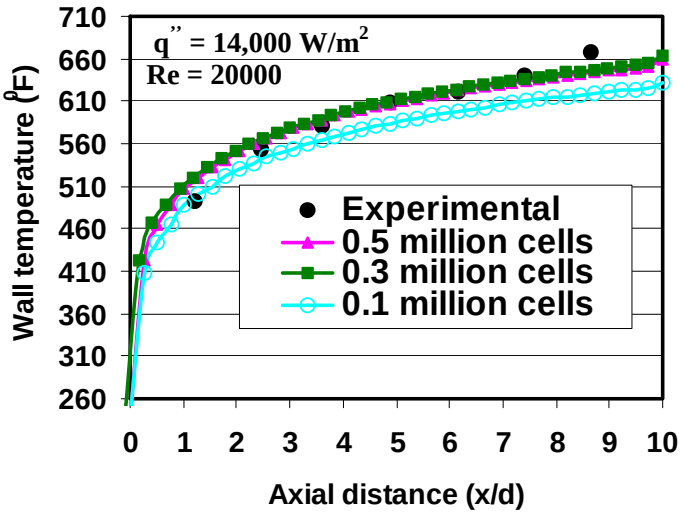

Figure 5 Grid sensitivity test (Steam only)

RESULTS AND DISCUSSION

Horizontal Tube with Steam-only Flow

Initially, the influence of turbulence models in predicting the wall temperature distributions has been tested for the flow conditions of Re = 20,000 and wall heat flux, q'' = 14,000 W/m^2. For this purpose, the turbulence models including Standard k-ε, RNG, Reynolds Stress Model (RSM), K-ω, and SST have been used. Figure 6 shows the predicted wall temperature values of each turbulence models considered against experimental values. The RSM and k-ε models have predicted the wall temperature values very close to the experimental values within 2% deviation. It should be noted that the experimental wall temperature measurement had an uncertainty of about 1.2% [8]. The RNG model provides the third best prediction. The K-ω, and SST models are less promising and show larger deviations from the experimental data. Considering the computational time required for RSM model being higher than the k-ε model, for the further computational investigation, k-ε model is used. The consistency of the k-ε model was checked at two lower wall heat flux cases including q'' = 9,000 and 5,000 W/m^2 against experimental values in Figs. 7a & b. Both cases confirm that the k-ε model satisfactorily predicts the wall temperature within 2% and heat transfer coefficient within 5% of the experimental data.

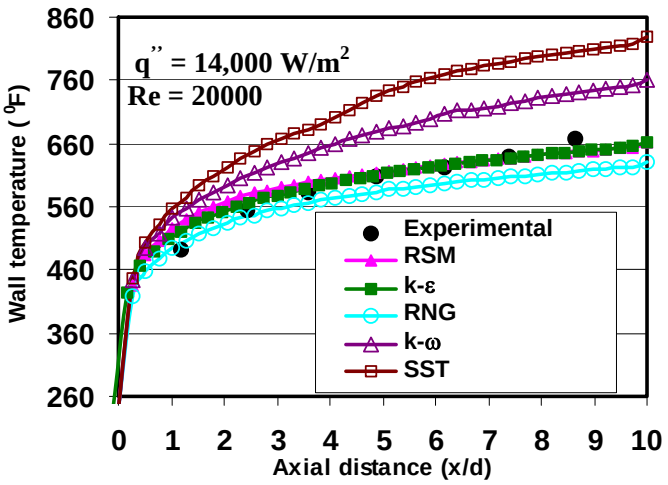

Figure 6 Effect of turbulence model on wall temperature distribution in steam-only flow. RSM and k-ε models provide the best results.

Horizontal Tube Simulation With Mist/Steam Flow

Effect of droplet diameter

After choosing the k-ε turbulence model for steam flow, computation is carried out to include the discrete phase of mist. The experiment result at a fixed measuring point at the tube inlet showed the mean droplet diameter of about 10μm. Taking the value as reference and assuming uniform droplet diameter at inlet, computation has been carried out for high heat flux case of q'' = 14,000 W/m^2 as shown in Fig. 8. The CFD result shows good match with experimental data at the entrance of pipe up to x/d = 2.5. Afterwards, the simulation underpredicts experimental wall temperature (or we shall say the simulation overpredicts the mist cooling effect) about 8% in the mid tube region and 25% at the exit of tube. Since it is known that small droplets evaporate faster than large droplets due to more surface area at a fixed mass flow rate, it was suspected that the droplets evaporate faster in the computation than in the experiment and hence the mist cooling effect is overpredicted (or the wall temperature is underpredicted) downstream of x/d = 2. To verify this speculation, computation has been carried out by increasing the droplet diameter from 10 μm to 20 μm (Fig. 8a). The result verifies that 20 μm droplets give less cooling enhancement, but the temperature is now overpredicted (or the mist cooling effect is underpredicted.) The evaporation rate of 10 μm and 20 μm droplets across the tube at x/d = 8 is shown in Fig. 8b. It can be seen that 10 μm droplets evaporate faster than the 20 μm droplets. Near the tube exit (x/d > 8), it seems either the mist has run low or only large droplets survive, 20 μm droplets case predicts better than 10 μm droplets.

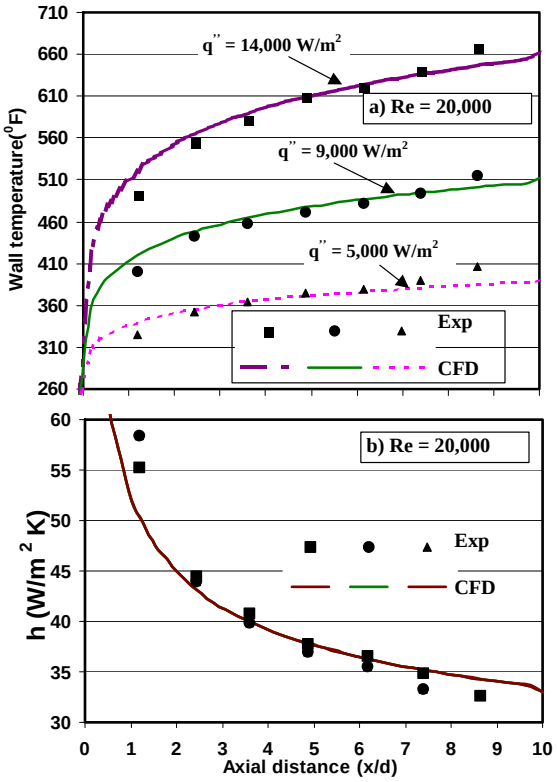

Figure 7 Wall temperature and heat transfer coefficient distributions for three different wall heat fluxes at Re = 20,000 of steam-only flow

Effect of droplet distribution

Realizing the effect of droplet diameter on the wall temperature and cooling effectiveness, calculations have been made for distributed droplet diameter varying from 5 μm to 50 μm with the mean diameter of about 10μm as

reported in the experimental studies [9]. The Rosin-Rammler distribution function is used which is based on the assumption that an exponential relationship exits between the droplet diameter, d_d, and the mass fraction of droplets with diameter greater than d, Y_d:

$$Y_d = e^{-(d/d_m)^n} \quad (27)$$

where d_m refers to the mean diameter and n refers to the spread parameter. Figure 9 shows the measured distribution of droplet diameter against experimental mass fraction obtained in [9]. From the relationship, the spread parameter (2.4) is calculated and used to fit the size distribution into the CFD model.

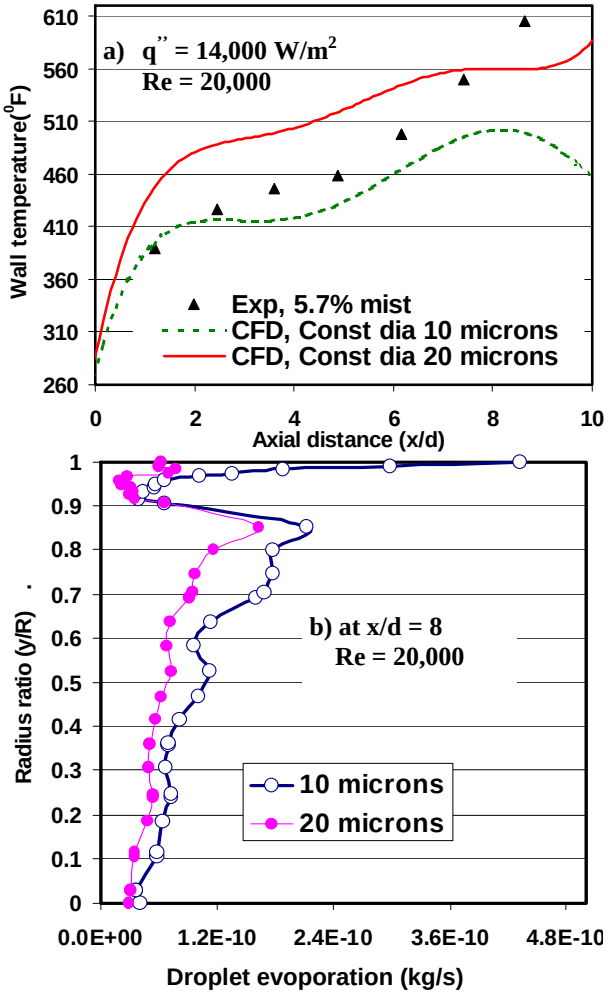

Figure 8 Effect of droplet

Figure 10 shows that the effect due to distributed droplet diameter is predominant in the entrance region up to x/d = 5 and insignificant half-way downstream the tube. The less than expected effect of droplet size distribution could be caused by the fact that the reported experimental droplet measurement was taken at a particular location near the tube inlet center and hence the results might not be a true representative of the droplet distribution across the tube. Therefore, a "reverse calibration" is attempted by changing the droplet diameters to match the experimental data. The computation is then carried out for another two distributed droplet sizes with the mean diameter of 15 and 20 μm, respectively. This approach is based on the reasoning that if by changing the droplet diameter can match the data well, at least many other models used in this simulation could be acceptable. Figure 11 shows the predicted wall temperature with distributed droplet diameter distribution with the mean diameter of 15 μm is found to be closer to the experimental results with the deviation of about 5% up to x/d = 8. But still the computational deviation at exit is as high as 13%.

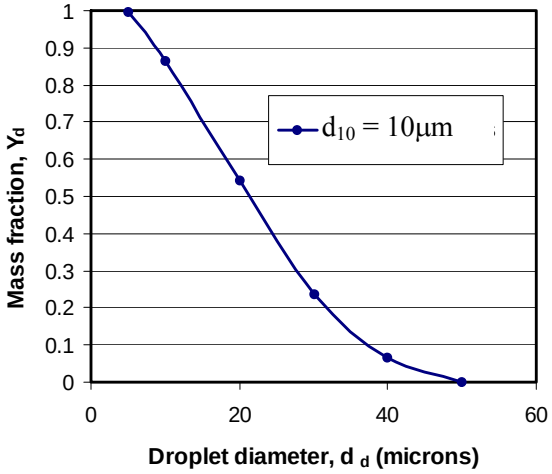

Figure 9 Using Rosin-Rammler distribution to fit the experimental droplet size distribution.

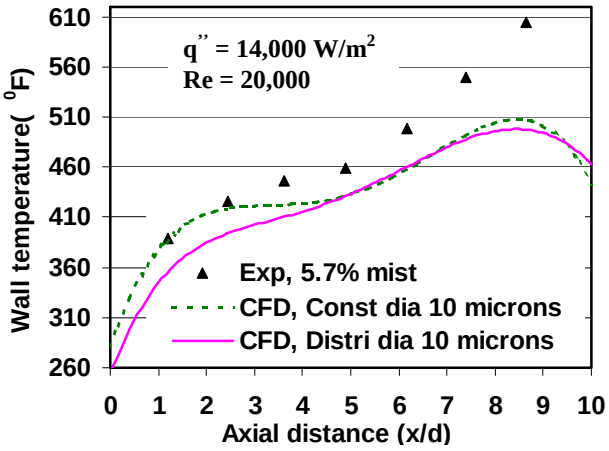

Figure 10 Effect of droplet distribution

Effect of discrete phase wall boundary condition

Two types of boundary conditions are considered including reflect and wall-film models. In the reflect model the change in the droplet momentum due to rebound after collision with the wall is calculated from the coefficient of restitution. The normal or tangential coefficient of restitution defines the amount of momentum normal or tangential to wall retains by the particle after collision with the wall [22]. The coefficients can be set to the function of impact angle of droplet with respect to the wall. In the present case as the droplets are transported parallel to the pipe wall, the impact angle would be small.

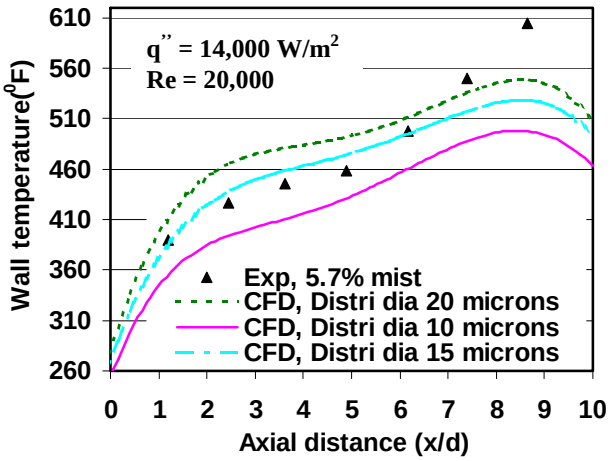

Figure 11 Effect of droplet mean diameter in the distribution function

On the other hand, the wall-film model addresses the issues including interaction during initial impact with wall boundary, subsequent tracking on surfaces, calculations of film variables and coupling to the continuous phase (steam) [22]. All the computational results discussed above uses the "reflect" wall condition, which do not model the wall film formation. In order to make the CFD model more robust, the wall-film model is included in all the simulations below. Figure 12 shows comparison of the wall temperature distribution between the reflect and wall film droplet model for the high heat flux case of q" = 14,000. The wall-film model predicts a bit closer to the experimental value than reflect wall model in the region up to x/d = 5. Overall speaking, both the model predicts approximately the same values, which suggests that the wall film might not form in this high heat flux case during the experiment. The model can be used to examine the low heat flux cases where the wall film might be formed due to water droplets deposition.

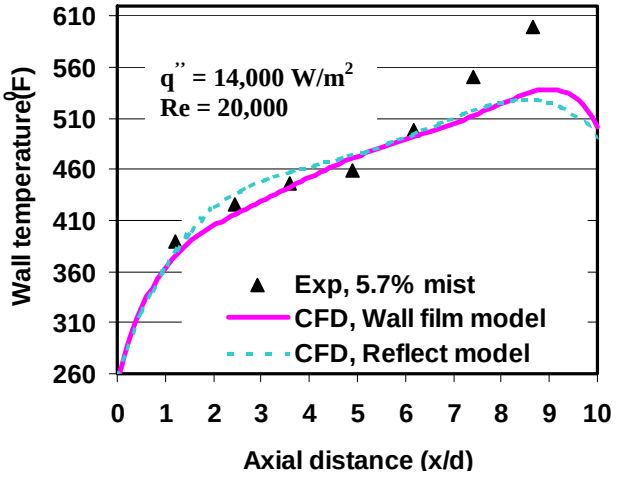

Figure 12 Effect of droplet-wall interaction models

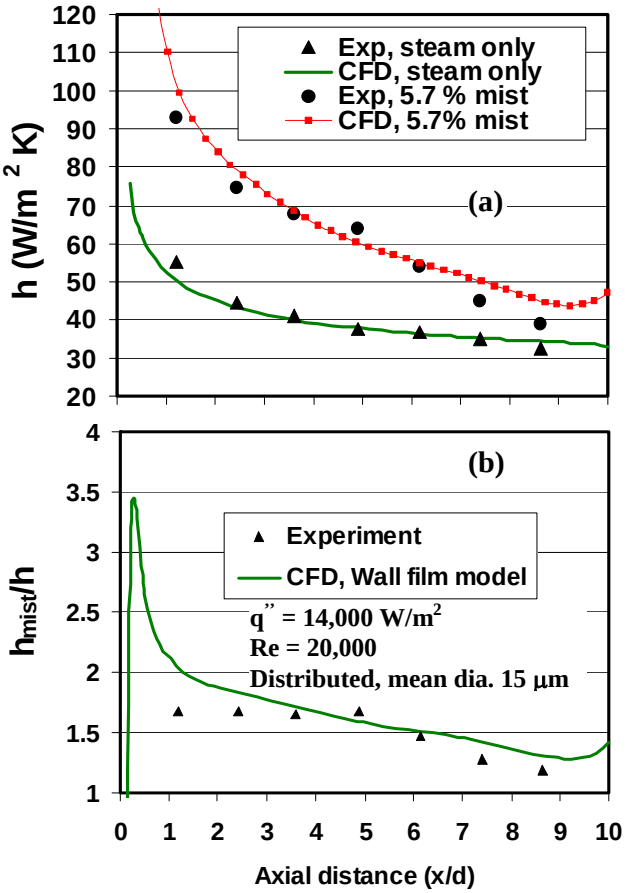

Figure. 13 Heat transfer results: a) heat transfer coefficient and b) cooling enhancement (ratio of heat transfer coefficient)

Distribution of heat transfer coefficient is plotted in Fig. 13a. Here, the heat transfer coefficient is calculated as:

$$h(x) = q''/(T_w(x)-T_{sat,in}) \quad (28)$$

The steam saturation temperature of 115^0C is taken as the inlet temperature and the constant wall heat flux is given as q" = 14,000 W/m^2. Figure 13a shows that the CFD model with wall-film model predicts the heat transfer coefficient of steam/mist flow satisfactorily in the mid portion of tube within 5% and at the inlet and exit portions within 12%. The computed and measured values of cooling enhancement (h_{mist}/h) are compared in Fig. 13b. It mostly reflects the deviation trend of h-values. The cooling enhancement, which involves the ratio of two heat transfer coefficients, is more sensitive to the inaccuracy of prediction. The cooling enhancement predicted by the CFD model in the first diameter of the pipe (x/d <1) is not trustful because no experimental data is available for comparison. Overall, the deviation is about 5% in predicting h-value and about 10% in predicting the cooling enhancement ratio.

The tuned CFD model has been used to examine the low heat flux case of 5,000 W/m^2 where the wall film might be formed due to water droplets deposition. Figure 14 confirms that the predicted wall temperature matches with

the experimental values within 7% deviation. The accuracy of prediction looks better than the high heat flux case of 14,000 W/m^2, especially at the downsteam region beyond x/d = 6.5. But the model did not predict the slight up-down-up nature, which was noticed in the experimental results. The figure shows steep temperature profile in the high heat flux case and almost flat profile in the low heat flux case in the region from x/b = 6 to 10. This shows that the cooling enhancement due to droplet reduces as the heat flux increases. In order to investigate the reason, droplet evaporation near the wall region at various axial locations has been plotted for the two heat flux cases as shown in Fig. 15. The figure shows zero evaporation at unheated and downstream region beyond x/d = 8.5 (shown in Fig. 17) for high heat flux case. This indicates that the droplets near the wall region have been completely evaporated when it reaches the location at about x/d = 8.5. This causes the low cooling enhancement region in the high heat flux case. In the low heat flux case, the evaporation rate is almost uniform throughout the heated portion in the near-wall region. Figure 16 shows the effective droplet evaporation region derived from Fig. 15 for the high and low heat flux cases. The red curve is drawn by connecting the locations where the droplet evaporation significantly increases in the radial direction. For example, in Fig. 15b, the y/R location where a drastic increase of evaporation rate at x/d = 8.5 is approximately at 0.98 which is correspondingly shown in Fig.16b. It can be noticed that very high evaporation rate occurs in the region of x/d = 1.5 to 5 in the high heat flux case. In this region, the droplets are expelled from the hot wall due to the effect of vapor layer created by intensive droplet evaporation. Due to a sudden addition of vapor mass to the continuous flow in the near-wall region, this effect of vapor expansion obstructs the path of oncoming droplets and results in few drops traveling in the continuous flow boundary layer at the far downsteam location. In comparison with the high heat flux case, the effective vapor expansion region in the low heat flux case is relatively flat. Figure 17 shows the evaporating rate at near-wall region (y/R = 0.99) for low and high heat flux cases and reveals that the maximum evaporation rate takes place at x/d = 3.5 and 1.5 for the high and low heat flux cases respectively. The abrupt reduction of droplet evaporation downstream of the maximum value can be clearly seen.

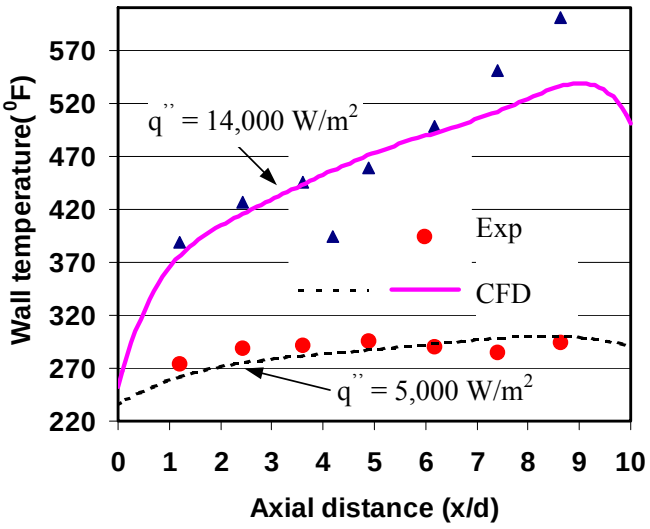

Figure 14 Validation at various wall heat flux cases

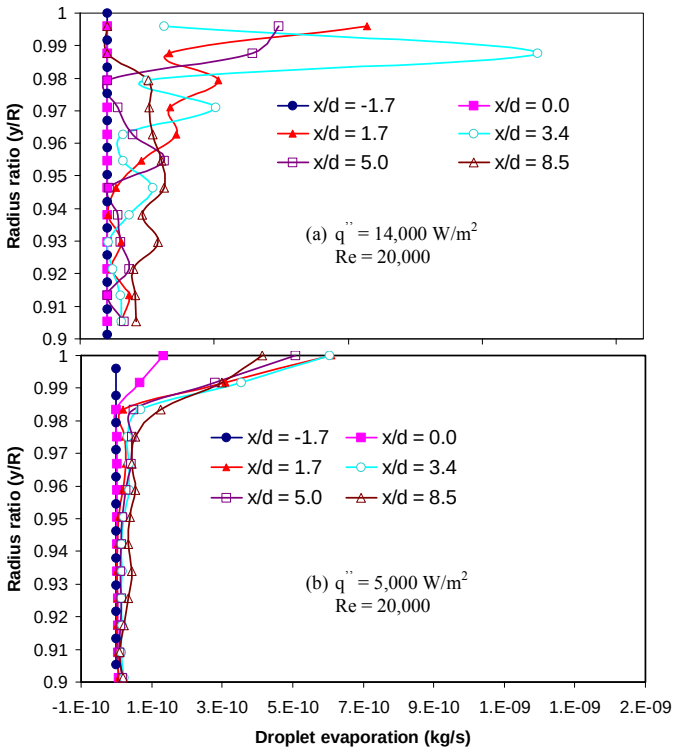

Figure 15 Droplet evaporation in the near- wall region. Negative x indicates unheated section upstream of the heated section.

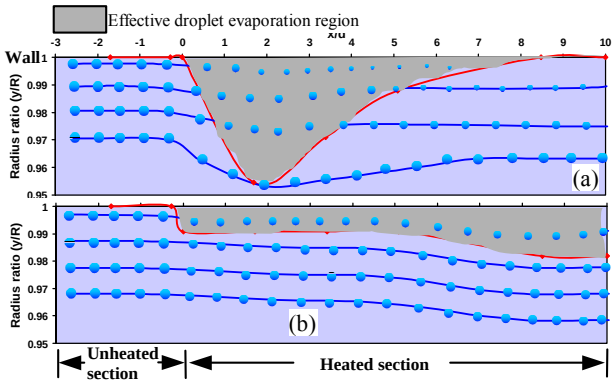

Figure 16 Near-wall effective droplet evaporation regions derived from Fig. 15: a) q'' = 14,000 W/m^2 and b) q'' = 5000 W/m^2

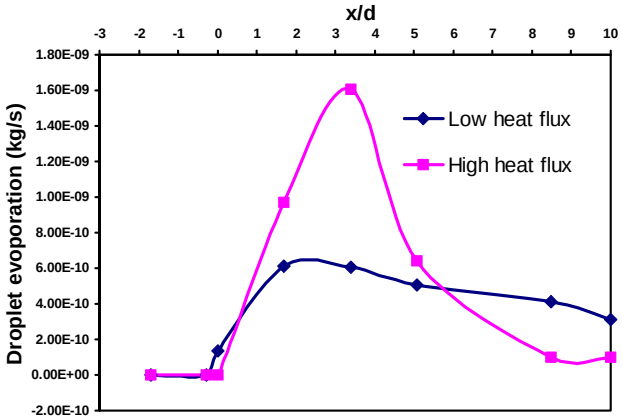

Figure 17 Near-wall accumulated droplet evaporation

Simulation Under Gas Turbine Operating Conditions at Elevated Pressure, Temperature, Heat flux, and Reynolds number

With sufficient confidence being built on the validation process against the laboratory experimental work under the low pressure, temperature, heat flux, and Reynolds number conditions, computation has been extended to simulate the mist cooling enhancement in real gas turbine environment under at elevated conditions. For this purpose the superheated steam at 1275 K and 15 atm pressure is chosen to reflect the actual gas turbine working condition. The wall heat flux and inlet velocity are increased from 14,000 to 140,000 W/m^2 and 12 m/s to 100 m/s, respectively (Re = 20,000 to 120,000). The mist ratio of 5.7% was maintained constant for both the cases. Table 1 gives the comparison of steam and water properties between low and elevated pressure and temperature conditions. The dynamic viscosity of steam increases about 3.9 times when the temperature increases from 388 K to 1275 K. The kinematic viscosity is related to the pressure through the density.

Table 1 Steam and water (liquid) properties at low and elevated conditions

Steam	388 K 1 atm	1275 K 15 atm
Density (kg/m^3)	0.7	2.58
Specific heat (J/kg-K)	2014	2488
Heat Conductivity (W/m-K)	0.0261	0.1369
Dynamic viscosity (kg/m-s)	1.24e^{-5}	4.78e^{-5}
Kinematic viscosity (m^2/s)	1.77e^{-6}	1.85e^{-6}
Water		
Saturation temperature (K)	373	472
Specific heat (J/Kg- K)	4180	4490
Density (kg/m^3)	998	866
Latent heat (KJ/kg)	1950	2260

Figures 18a and b show comparison of the temperature and heat transfer coefficient distributions between steam-only and mist/steam flows at elevated operating conditions. Considerable reduction in the wall temperature can be seen due to mist cooling in Fig. 18a. The effect of mist cooling can be seen in the heat transfer coefficient in Fig. 18b. The average increase in heat transfer coefficient of about 200% is noted at elevated operating conditions, whereas in low operating conditions, the enhancement ratio is about 30% - 60% (see Fig. 13b). Figure 19 further testifies that the mist cooling enhancement ranging from about 500% near x/d=1 to about 30% at x/d= 8. If sufficient mist is provided, it suffices to state that mist cooling can provide approximately 50%-100% average cooling enhancement in a horizontal tube under real gas turbine operating condition. The reason for the better cooling performance at elevated operating conditions may be due to the high inlet velocity (Reynolds number) and increased heat capacity and latent heat which result in a better mist transportation and better medium to serve as a heat sink for absorbing heat. It needs to be noted that heat transfer of steam-only flow is also benefited from high speed and more favorable properties in real gas turbine conditions; however, it seems mist cooling gains more.

The cooling enhancement in the experiments conducted by Guo et al. [9] showed that the mist cooling enhancement deteriorated when wall heat flux increased. It was concerned then that the mist cooling might not be beneficial under the elevated wall heat flux condition in the real gas turbine operating environment. At that time, Guo et al, speculated that the mist cooling could be still attractive under gas turbine operating condition because the Reynolds number is high and the steam properties will change in favor of mist cooling. This study supports their earlier speculation. The current authors feel fairly comfortable with the predicted result under the elevated gas turbine operating conditions based on the following reasons: (a) The major models such as turbulence, forces on droplets, heat and mass transfer, droplet wall boundary condition have been verified with the experimental data. (b) Although the condition is under low pressure and temperature, the verification process at least shows these models perform satisfactorily and no big problems exist. (c)

Considering the physics involved in these models, it is unlikely that they will be significantly affected by the elevated conditions except the thermodynamic properties which should be adequately carried out by the property tables in the CFD model. Therefore, the trend of the results in this study under elevated conditions should be trustful.

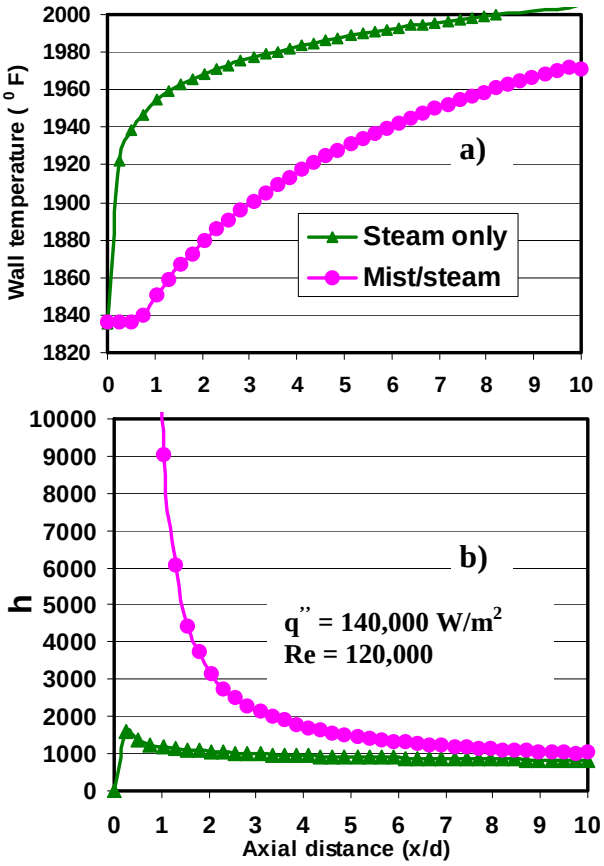

Figure 18 Heat transfer results at elevated operating conditions: a) wall temperature and b) heat transfer coefficient (W/m^2 K)

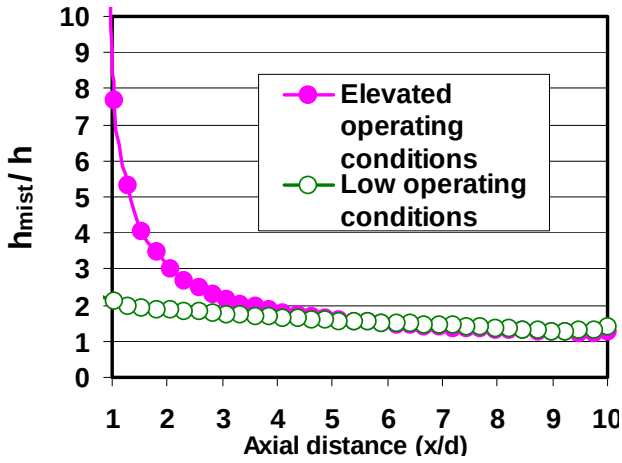

Figure 19 Comparison of cooling enhancement (h_{mist}/h) at high and low operating conditions

CONCLUSIONS

A CFD model has been validated against the available experimental results of mist/steam cooling in a heated horizontal tube. The following conclusions are drawn:

- The validation process reveals that the RSM and k-ε models with enhanced wall functions provides better results on this application than other turbulent models.
- In steam-only flow, the CFD model successfully predicts the wall temperature within 2% and h-values within 5% from the experimental results
- In the mist flow, by increasing the droplet mean diameter from the experimental value of 10 μm to 15 μm, the CFD model satisfactorily predicts the wall temperature and h-values within 5%, and cooling enhancement within 10% from the experimental results except near inlet and exit of the heated tube.
- The wall-film model has been successfully implemented in the CFD model and it predicts slightly better than the reflect model in higher wall heat flux condition.
- The accuracy of temperature prediction increases as the heat flux increases which was particularly noticed at the far field of the hot surface.
- The validated CFD model has been used to predict the mist/steam cooling under real gas turbine operating conditions and noted that the mist cooling works better in elevated temperature, pressure , heat flux, and Reynolds number conditions than in the low operating condition. The average cooling enhancement of 200% was noted in the elevated operating condition versus 40% in the corresponding low pressure and temperature operating condition.

ACKNOWLEDGEMENTS

This study was supported by the Louisiana Governor's Energy Initiative via the Clean Power and Energy Research Consortium (CPERC) and administered by the Louisiana Board of Regents.

NOMENCLATURE

d	diameter of tube (m)
C	concentration (kg/m^3)
h	convective heat transfer coefficient(W/m^2-K)
k	turbulent kinetic energy (m^2/s^2)
k_c	mass transfer coefficient
K	thermophoretic coefficient
m	mass (kg)
q''	wall heat flux (W/m^2)
Re	Reynolds number
T_w	wall temperature (^{o}C)
$T_{sat,in}$	inlet temperature (^{o}C)
v	velocity (m/s)

Greek

ε	turbulence dissipation (m^2/s^3)
λ	thermal conductivity (W/m-K)

Subscript

p or d	particle or droplet

REFERENCES

[1] Van der Lindea, S., 1992, "Advanced Turbine Design Program," Proc. Ninth Annual Coal-Fueled Heat Engines, Advanced Pressurized Fluid-Bed Combustion (PFBC), and Gas Stream Cleanup Systems Contractors Reviewing Meeting, Oct. 27-29, Morgantown, WV, pp.215-227.

[2] Bannister, R. L., and Little, D. A., 1993, "Development of Advanced Gas Turbine System," Proc. Joint Contractor Meeting: FE/EE Advanced Turbine System Conference; FE Fuel cells and Coal-Fired Heat Engines Confence, Aug 3-5, Morgantoown, WV, pp. 3-15.

[3] Mukavetz, D. W., Wenglarz, R., Nirmalan, M., and Daehler, T., 1994, "Advanced Turbine System (ATS) Turbine Modification for Coal and Biomas Fuels," Proc. Of the Advanced Turbine System Annual Program Review Meeting, Nov. 9-11, ORNL/Arlington, VA, pp. 91-95.

[4] Bannister, R. L., Cheruvu, N. S., Little, D. A., and McQuiggan, G., 1995, "Development Requirements for an Advanced Gas Turbine System," ASME J. Turbomach., 117, pp. 724-733.

[5] Farmer, R., and Fulton, K., 1995, "Design 60% Net Efficiency in Frame 7/9H Steam-Cooled CCGT," Gas Turbine World, May-Jun, pp. 12-20.

[6] Mukherjee, D., 1984, "Combained Gas Turbine and Steam Turbine Power Station," Patented by ABB, US. Patent No. 4424668.

[7] Alff, R. K., Manning, G. B., and Sheldon, R. C., 1978, "The High Temperature Water Cooled Gas Turbine in Combained Cycle with Integrated Low BTU Gasificatoin," Combustion, 49, pp. 27-34.

[8] Guo, T., Wang, T., and Gaddis, J. L., 2000, "Mist/Steam Cooling in a Heated Horizontal Tube: Part 1: Experimental System," ASME J. Turbomachinery, 122, pp. 360-365.

[9] Guo, T., Wang, T., and Gaddis, J.L., 2000, "Mist/Steam Cooling in a Heated Horizontal Tube: Part 2: Results and Modelling," ASME J. Turbomachinery, 122, pp. 366-374.

[10] Guo, T., Wang, T., and Gaddis, J. L., 2000, "Mist/Steam Cooling in a 180-Degree Tube," ASME J. Heat Transfer, 122, pp. 749-756.

[11] Li, X., Gaddis, T., and Wang, T., 2001, "Mist/Steam Heat Transfer of Confined Slot Jet Impingement," ASME J. Turbomachinery, 123, pp. 161-167.

[12] Li, X., Gaddis, J. L., and Wang, T., 2003, "Mist/Steam Heat Transfer With Jet Impingement onto a Concave Surface," ASME J. Heat Trasnfer, 125, pp.438-446.

[13] Styrikovich, M. A., Polonsky, G. V.,and Tsiklaury, G. V., 1982, "Heat and Mass Transfer and Hydrodynamics in Two-Phase Flows of Nuclear Power Station," Nauka, Moscow, Russia.

[14] Hodgson, J. W., Saterbak, R. G., and Sunderland, J. E., 1968, "An Experimental Investigation of Heat Transfer from a Spray Cooled Isothermal Cylinder," ASME J. Heat Transfer, 90, 4, pp. 457-463.

[15] Aihara, T., Taga, M., and Haraguchi, T., 1979, "Heat Transfer from a Uniform Heat Flux Wedge in Air-Water Mist Flow," Int. J. Heat and Mass Transfer, 22, 1, pp. 51-60.

[16] Hishida, K., Maeda, and M., Ikai, S., 1980, "Heat Trasnfer from a Flat Plate in Two-Component Mist Flow," ASME J. Heat Trasnfer, 102, 3, pp. 513-518.

[17] Terekhov, V. I., and Pakhomov, M. A., 2002, "Numerical Study of Heat Transfer in a laminar Mist Flow over a Isothermal Flat Plate," Int. J. Heat Mass Transfer, 45, 10, pp. 2077-2085.

[18] Koizumi, Y., Ueda, T., and Tanaka, H., 1979, "Post Dryout Heat Transfer to R-113 Upward Flow in a Vertical Tube," Int. J. Heat Mass Transfer, 22, 8, pp. 669-678.

[19] Rane, A. G.,and Yao, S. Ch., 1981, "Convective Heat Transfer to Turbulent Droplet Flow in Circular Tubes," ASME J. Heat Transfer, 103, 4, pp. 679-684.

[20] Launder, B. E., and Spalding, D. B., 1972, Lectures in Mathematical Models of Turbulence, Academic Press, London, England.

[21] Wolfstein, M., 1969, "The Velocity and Temperature Distribution of one-Dimensional Flow with Turbulence Augmentation and Pressure Gradient," Int. J. Heat Mass Transfer, 12, pp. 301-318.

[22] Fluent Manual, Version 6.2.16, 2005, Ansys Inc.

[23] Choudhury, D., 1993, "Introduction to the Renormalization Group Method and Turbulence Modeling," Technical Memorandum, TM-107, Fluent Inc.

[24] Wilcox, D. C., 1998, "Turbulence Modeling for CFD," DCW Industries, Inc., La Canada, California.

[25] Menter, F., 1993, "Zonal Two Equation Model for Aerodynamics Flows," AIAA paper 93-2906.

[26] Saffman, P. G., 1965, "The Lift on a small Sphere in a Slow Shear Flow," J. Fluid Mech., 22, pp. 737-758.

[27] Talbot, L., Cheng, R. K., Schefer, R. W., and Willis, D. R., 1980, "Thermophoresis of Particles in a Heated Boundary Layer," J. Fluid Mech., 101, pp. 737-758.

[28] Li, A., and Ahmadi, G., 1992, "Dispersion and Deposition of Spherical Particles from Point Sources in a Turbulent Channel Flow," Aerosol Science and Technology, 16, pp. 209-226.

[29] Ranz, W. E., and Marshall, W. R. Jr., 1952, "Evaporation from Drops, Part I," Chem. Eng. Prof., 48, pp. 141-146.

[30] Ranz, W. E., and Marshall, W. R., Jr., 1952, "Evaporatin from Drops, Part II," Chem. Eng. Prof., 48, pp. 173-180.

[31] Kuo, K. Y., 1986, Principles of Combustion, John Willey and Sons, New York.

[32] Watchers, L. H. J., and Westerling, N. A., 1966, "The Heat Transfer from a Hot Wall to Impinging Water Drops in the Spherioidal State," Chem. Eng. Sci., 21, pp. 1047-1056.

[33] Harlow, F. H., and Shannon, J. P., 1967, "The Splash of a Liquid Drop," Journal of Applied Physics, 38, 10, pp. 3855-3866.

[34] Bai, C., and Gosman, A. D., 1995, "Development of Methodology for Spray Impingement Simulation," SAE Paper 950283.

[35] Yarin, A. and Weiss, D. A., 1995, "Impact of Drops on Solid Surfaces: Self-Similar Capillary Waves, and Splashing as a New Type of Kinematic Discontinuity," J. Fluid Mech., 283, pp. 141-173.

[36] Stow, C. D., and Stainer, R. D., 1977, "The Physical Products of a Splashing Water Drop," Journal of the Meteorological Society of Japan, 55, 5, pp. 518-531.

[37] Stanton, D. W., and Rutland, C. j., 1996, "Modeling Fuel Film Formation and Wall Interaction in Diesel Engines," SAE Paper 960628.

[38] Rourke, P. J. O., and Amsden, A. A., 2000, "A Spray/Wall Interaction Submodel for the KIVA-3 Wall Film Model," SAE Paper 2000-01-0271.

[39] Wang, T. and Dhanasekaran, T. S., 2008, "Calibration of CFD Model for Mist/Steam Impinging Jets Cooling," ASME Paper GT2008-50737, Turbo Expo2008, Berlin, Germany, June 9-13, 2008.